Remimazolam attenuates myocardial ischemia/reperfusion injury by inhibiting ferroptosis involving the AKT/SLC7A11/GPX4 axis

XIYUAN CHEN[1*], JIANGHONG ZHAO[1*], XINGTONG HE[2], YUQI ZHANG[1], JIAO WU[1], CHAO JIANG[1], YI YANG[2] and JI XIAO[1]

[1]Department of Anesthesiology, The Affiliated Cancer Hospital of Xiangya School of Medicine, Central South University, Changsha, Hunan 410013, P.R. China; [2]Department of Anesthesiology, The Second Affiliated Hospital of University of South China, Hengyang, Hunan 421001, P.R. China

Received May 14, 2026; Accepted August 21, 2026

DOI: 10.3892/ijmm.2026.5998

Abstract. Remimazolam (RMZ) is an ultra-short-acting sedative anesthetic that provides protection against cerebral and hepatic ischemia/reperfusion injury. However, its potential cardioprotective effect in myocardial ischemia reperfusion injury (MIRI) remains to be fully elucidated. The present study investigated the hypothesis that RMZ can mitigate MIRI, clarifying its underlying mechanisms. Using a mouse MIRI model, the effects of RMZ on cardiac function, cell death, lipid peroxidation, Fe^{2+} accumulation and ferroptosis-related markers were assessed, together with transmission electron microscopy (TEM) imaging. Transcriptomic analysis identified ferroptosis signatures in cardiomyocytes (CMs). Ferrostatin-1 (Fer-1) served as a positive control to validate the anti-ferroptotic effects of RMZ. Additional mechanistic studies were conducted with H9C2 cells subjected to oxygen-glucose deprivation/reoxygenation (OGD/R) to evaluate cell death, lipid peroxidation, Fe^{2+} accumulation, TEM and the signaling pathways involved. In the MIRI model, mice treated with RMZ exhibited greater resistance to MIRI, as evidenced by improved cardiac function, reduced myocardial injury markers and decreased TUNEL-positive CMs. Transcriptomic analysis indicated the activation of ferroptosis following MIRI. Furthermore, RMZ and Fer-1 inhibited Fe^{2+} accumulation, restored glutathione (GSH) levels, enhanced glutathione peroxidase 4 (GPX4) expression and alleviated mitochondrial ferroptosis damage. In the OGD/R model using H9C2 cells, RMZ normalized Fe^{2+}, GSH and GSH/oxidized GSH levels, decreased peroxidase activity and reduced OGD/R-induced ferroptosis, which was associated with the restoration of the protein kinase B (AKT)/solute carrier family 7 member 11 (SLC7A11)/glutathione peroxidase 4 (GPX4) axis. These findings demonstrated that RMZ protects against MIRI by inhibiting ferroptosis that involves the activation of the AKT/SLC7A11/GPX4 signaling cascade, highlighting its therapeutic potential for improving cardiac outcomes following reperfusion injury.

Correspondence to: Professor Ji Xiao, Department of Anesthesiology, The Affiliated Cancer Hospital of Xiangya School of Medicine, Central South University, 283 Tongzipo Road, Yuelu, Changsha, Hunan 410013, P.R. China
E-mail: 253477652@qq.com

Professor Yi Yang, Department of Anesthesiology, The Second Affiliated Hospital of University of South China, 35 Jiefang Avenue, Zhengxiang, Hengyang, Hunan 421001, P.R. china
E-mail: yangyi@usc.edu.cn

*Contributed equally

Key words: remimazolam, cardioprotection, myocardial ischemia reperfusion injury, ferroptosis

Introduction

Cardiovascular diseases remain the leading cause of global mortality, with acute myocardial infarction (MI) contributing markedly to these deaths (1). Timely restoration of coronary blood flow through primary percutaneous coronary intervention or thrombolysis constitutes the cornerstone of modern MI therapy; however, reperfusion paradoxically triggers myocardial ischemia-reperfusion injury (MIRI), markedly diminishing the benefits of revascularization (2). MIRI is characterized by a self-amplifying cascade involving a reactive oxygen species (ROS) burst, intracellular Ca^{2+} overload, mitochondrial energetic failure and sterile inflammation, ultimately leading to cardiomyocyte death and impaired cardiac function. Despite decades of intensive research, no targeted intervention for MIRI has been successfully translated into routine clinical practice, highlighting the urgent need for novel cardioprotective strategies.

Ferroptosis, a recently identified form of iron-dependent regulated necrosis driven by lethal lipid peroxidation, has emerged as a critical mediator of reperfusion-induced tissue damage across multiple organ systems (3-5). This unique cell death pathway is tightly regulated by the cystine-glutamate antiporter SLC7A11 (system Xc-), which maintains intracellular glutathione (GSH) levels by mediating cystine uptake. GSH serves as a cofactor for glutathione peroxidase 4 (GPX4), an enzyme that neutralizes lipid hydroperoxides and prevents ferroptotic cell death. Disruption of the SLC7A11-GSH-GPX4

axis, through cystine deprivation, GSH depletion, or direct GPX4 inactivation, leads to the accumulation of labile iron and lipid peroxides, culminating in plasma membrane rupture and cell death (5,6). Evidence implicates ferroptosis in the pathogenesis of acute kidney injury, neurodegenerative disorders and ischemic stroke (7-10), with pharmacological inhibition consistently attenuating experimental ischemia/reperfusion (I/R) injury (11). However, the precise role and therapeutic potential of targeting ferroptosis in MIRI remain incompletely defined, representing a critical knowledge gap in the field.

Remimazolam (RMZ), an ultra-short-acting benzodiazepine, functions as a high-affinity, selective agonist at γ-aminobutyric acid type A (GABA_A) receptors and is widely used for procedural sedation, general anesthesia induction/maintenance and intensive care unit sedation (12-16). Beyond established sedative-hypnotic properties (17,18), emerging preclinical evidence suggests that RMZ may exert pleiotropic organ-protective effects. Animal studies have shown that RMZ mitigates cerebral and hepatic I/R injury by suppressing oxidative stress and apoptosis (19-23). However, whether RMZ confers cardioprotection against MIRI and if this effect involves modulation of ferroptosis, remains unknown. The present study systematically evaluated the cardioprotective efficacy of RMZ using a murine model of coronary artery ligation/reperfusion and a cardiomyocyte OGD/R model, while exploring its underlying mechanisms.

Materials and methods

Animals. Specific pathogen-free C57BL/6J wild-type male mice (8-10 weeks old, 22-25 g) were obtained from Beijing Vital River Laboratory Animal Technology Co., Ltd. A total of 50 mice were housed in groups of five per cage in a specific pathogen-free environment, maintained under controlled temperature of 22-24˚C and relative humidity of 50-60%, with a 12-h light/dark cycle, with access to standard chow and sterile water. The present study was approved by the Institutional Animal Ethics Committee at The Affiliated Cancer Hospital of Xiangya School of Medicine and adhered to the National Institutes of Health Guide for the Care and Use of Laboratory Animals (8th edition, 2011; https://www.ncbi.nlm.nih.gov/books/NBK54050/) Randomization was conducted using a computer-generated random number table, ensuring group allocation was concealed in sealed opaque envelopes opened immediately prior to surgery. All outcome assessments were performed by investigators blinded to group allocation. Mice were randomly assigned to five groups: Sham, RMZ, I/R, I/R + RMZ and I/R + Fer-1. All mice were anesthetized with 2.5% isoflurane for induction and 1.5-2% isoflurane for maintenance (RWD Life Science Co., Ltd.) for the same duration and underwent identical surgical procedures, excluding LAD ligation. To minimize potential confounding due to the anesthetic agent, all groups received an identical isoflurane regimen and comparable surgical exposure time, ensuring that intergroup differences were attributable to the interventions and not variations in anesthesia. The Sham and RMZ groups underwent thoracotomy without ligation of the left anterior descending coronary artery (LAD), while I/R group mice underwent LAD ligation, inducing 30 min of ischemia followed by 24 h of reperfusion to establish a mouse model of left ventricular anterior wall MIRI. Successful ischemia was confirmed by visible blanching of the left ventricular anterior wall upon LAD ligation and successful reperfusion was indicated by a rapid return of color (flush) upon release of the ligature. Mice in the RMZ and I/R + RMZ groups received an intraperitoneal injection of 15 mg/kg RMZ (Jiangsu Hengrui Pharmaceutical Co., Ltd.) before reperfusion, while mice in the I/R + Fer-1 group were injected with 1 mg/kg Ferrostatin-1 (Fer-1; cat. no. HY-151563; MedchemExpress) prior to reperfusion; 0.9% normal saline served as the control in the Sham and I/R groups. Dosages of RMZ and Fer-1 were based on previous literature (24,25). Mice were euthanized immediately after 24 h of reperfusion by intraperitoneal injection of an overdose of sodium pentobarbital (150 mg/kg; cat. no. P3761; MilliporeSigma). Death was confirmed by i) absence of spontaneous respiration and heartbeat for at least 2 min, ii) bilateral pupil dilation and iii) absence of response to toe pinch.

The sample size was determined based on preliminary experiments and reference to published data from comparable models, ensuring adequate statistical power. Animals were excluded if they i) died during surgery or reperfusion, or ii) failed LAD ligation. During model construction, one mouse in the I/R group and one in the I/R + RMZ group died unexpectedly due to pneumothorax, while no mortality occurred in the Sham or RMZ groups. Animals meeting humane endpoints (persistent bradycardia, gasping, or loss of righting reflex) were immediately sacrificed and excluded from final analysis, with no animals meeting humane endpoints prior to the scheduled endpoint. The final sample size of n=6 per group for outcome analyses reflects animals that successfully completed the protocol without exclusion.

After reperfusion, hearts were rapidly excised and rinsed in ice-cold PBS. The left ventricle was carefully dissected, with the ischemic/infarcted zone defined as the myocardium distal to the LAD ligation suture, appearing pale and dyskinetic with clear demarcation from well-perfused adjacent tissue. This area was meticulously separated from the non-ischemic portion. The same cohort of surviving animals was used for all outcome measurements, with tissue samples allocated according to the requirements of each assay.

Echocardiography. Cardiac function was meticulously recorded and analyzed using a VisualSonics® Vevo3100® ultra-high resolution small animal ultrasound system (VisualSonics, Inc.). Initially, the B-mode ultrasound image of the long-axis section (LAX) of the left ventricle was obtained. The probe was then rotated 90˚ to acquire a short-axis section (SAX) view of the left ventricular papillary muscles, from which an M-mode ultrasound image was derived. Parameters including left ventricular fractional shortening (FS), ejection fraction (EF), left ventricular end-diastolic dimension (LVEDD) and left ventricular end-systolic dimension (LVESD) were calculated. The heart rate of control mice was recorded at 450±20 beats per min.

Hematoxylin and eosin staining. Cardiac tissues were fixed in 4% paraformaldehyde at 4˚C for 24 h, then dehydrated through a graded alcohol series (70, 80, 95 and 100% ethanol; 1 h each), cleared in xylene (two changes, 1 h each), embedded in paraffin wax, and sectioned at 5 μm. Sections were stained

with hematoxylin for 10 min at room temperature, rinsed in running water for 2 min and differentiated in 1% hydrochloric acid alcohol for 30 sec. After a water wash, counterstaining was performed with eosin for 5 min. Dehydration of the sections took place through a graded alcohol series, followed by clearing in xylene and mounting. Histological assessment focused on qualitative evaluation of myofibrillar architecture, interstitial edema and cytoplasmic vacuolation.

Immunofluorescence. Tissue fixation, embedding, and sectioning were performed as described above for hematoxylin and eosin staining. Sections were subjected to antigen retrieval using an appropriate buffer to expose epitopes for antibody binding at 95˚C for 15 min. Blocking was performed with 10% normal goat serum (1:20; cat. no. SL038; Beijing Solarbio Science & Technology Co., Ltd.) diluted in phosphate-buffered saline (PBS) for 1 h at room temperature to minimize non-specific binding. Primary antibodies were applied overnight at 4˚C to enhance binding affinity. Following incubation, sections were washed three times with PBS for 10 min each to remove unbound antibodies. Secondary antibodies were then applied for 1 h at room temperature. The antibodies utilized included 4-Hydroxynonenal (4-HNE; mouse; 1:100; cat. no. 68538-1-Ig; Proteintech Group, Inc.) and wheat germ agglutinin (WGA; cat. no. FL-1021; Vector Labs), as well as goat anti-mouse Alexa Fluor 594 (1:200, cat. no. A-11005; Invitrogen; Thermo Fisher Scientific, Inc.). Nuclei were counterstained with DAPI (1 μg/ml; cat. no.C0065; Beijing Solarbio Science & Technology Co., Ltd.) for 5 min at room temperature. For histological and immunofluorescence analyses, three non-consecutive sections per heart were evaluated and five randomly selected fields per section were analyzed at x20 magnification. All quantifications were performed using ImageJ software (version 1.53K; National Institutes of Health) by investigators blinded to group allocation.

TUNEL staining protocol. Following deparaffinization in xylene and rehydration through a graded ethanol series, tissue sections were treated with 20 μg/ml DNase-free Proteinase K at 37˚C for 30 min. After three washes with 1X PBS for 5 min each, the TUNEL reaction mixture (cat. no. C1089; Beyotime Biotechnology) was applied. Sections were incubated with the mixture at 37˚C in the dark for 60 min, followed by three washes with 1X PBS. Counterstaining with DAPI for 5 min at room temperature was performed and the sections were mounted with an anti-fade mounting medium.

Western blotting. Proteins were extracted from tissues and cells utilizing RIPA lysis buffer supplemented with protease inhibitors. Protein concentration was determined using the BCA assay (cat. no. 23225; Thermo Fisher Scientific, Inc.). Equal amounts of protein (20 μg per lane) were then separated by 15% SDS-PAGE and transferred to nitrocellulose membranes. Following a blocking step with 5% skimmed milk for 2 h at room temperature, membranes were incubated overnight at 4˚C with primary antibodies specific to β-actin (cat. no. 66009-1-Ig; 1:20,000; Proteintech Group, Inc.), β-Tubulin (cat. no. 10094-1-AP; 1:20,000; Proteintech Group, Inc.), p-Akt (Ser473) (cat. no. 9271; 1:1,000, CST, Danvers, MA, USA), Akt (cat. no. 9272; 1:1,000; Cell Signaling Technology, Inc.), SLC7A11 (cat. no. A03036-2; 1:1,000; Wuhan Boster Biological Technology, Ltd.), GPX4 (cat. no. DF6701; 1:1,000, Affinity) and proliferating cell nuclear antigen (PCNA, cat. no. 10205-2-AP; 1:5,000; Proteintech Group, Inc.). Following primary antibody incubation, membranes were treated with HRP-conjugated secondary antibodies (HRP-conjugated Goat Anti-Mouse IgG, cat. no. SA00001-1. HRP-conjugated Goat Anti-Rabbit IgG, cat. no. SA00001-2; 1:5,000; Proteintech Group, Inc.) for 2 h at room temperature. Protein bands were visualized using an ECL reagent (cat. no. SQ201; Epizyme Biomedical Technology Co., Ltd., Shanghai, China) and imaging was performed with a ChemiDoc XRS Plus system (Bio-Rad Laboratories, Inc.). Densitometric analysis was performed using ImageJ software (version 1.53k; National Institutes of Health).

Transcriptomic data source. The present study obtained two MIRI-related datasets, GSE141512 (human) (26) and GSE160516 (mouse, http://www.ncbi.nlm.nih.gov/geo), from the Gene Expression Omnibus (GEO) database (http://www.ncbi.nlm.nih.gov/geo). GSE141512 includes peripheral blood mononuclear cells transcriptomic profiles from six control subjects and six patients with acute MI, profiled on the GPL10558 platform (Illumina HumanHT-12 V4.0 expression beadchip; Illumina, Inc.). GSE160516 consists of left ventricular tissue transcriptomic profiles from four sham-operated mice and four mice subjected to MIRI, profiled on the GPL24247 platform (Illumina NovaSeq 6000, *Mus musculus*; Illumina, Inc.). No batch correction was necessary as each dataset was independently analyzed. For both datasets, probe IDs were converted to gene symbols and expression data were $\log_2$-transformed and quantile-normalized. Differential expression analysis was performed on the normalized gene expression profiles using R software (https://www.r-project.org/; limma package, version 3.26.9). Genes with $|\log_2\text{FoldChange (FC)}| \geq 0.5$ and FDR <0.05 were classified as differentially expressed genes (DEGs). Gene expression heatmaps and volcano plots were generated using the Sangerbox online platform (http://vip.sangerbox.com/).

Identification of DEGs and ferroptosis-related genes (FRGs). To compile a comprehensive list of FRGs, gene sets were integrated from three sources: the FerrDb database (version V2, 2022; http://www.zhounan.org/ferrdb/), the GOBP_FERROPTOSIS (M46862) gene set and the WP_FERROPTOSIS (M39768) gene set from the Molecular Signatures Database (https://www.gsea-msigdb.org; version 2026.1). After removing duplicates, a unified list of 731 FRGs was compiled for subsequent analyses. The VennDiagram package in R software (https://cran.r-project.org/package=VennDiagram; version 1.8.2) was utilized to identify the intersection between DEGs and FRGs, with overlapping genes defined as differentially expressed FRGs (DEFRGs).

Functional enrichment analysis. Gene Ontology (GO) and Kyoto Encyclopedia of Genes and Genomes (KEGG) enrichment analyses of the identified DEFRGs were conducted using the DAVID online tool (http://david.ncifcrf.gov/). Statistical significance was determined by adjusted P-values (q-values)

calculated using the Benjamini-Hochberg method (27) to correct for multiple hypothesis testing. GO terms and KEGG pathways with q<0.05 were considered markedly enriched.

Gene set enrichment analysis (GSEA). The association between cardiac transcriptomes and the FRG set was explored using the GSEA tool available on the Sangerbox website (http://vip.sangerbox.com/). Gene expression values in the dataset were ranked and scored to calculate the FDR and normalized enrichment score (NES). An FDR <0.05 and |NES|>1 were considered statistically significant.

Transmission electron microscopy (TEM). Mouse left ventricular myocardium or H9C2 cells were fixed in 2.5% glutaraldehyde (0.1 M phosphate buffer, pH 7.4) overnight at 4˚C. Cells were additionally scraped and pelleted. After washing, samples were post-fixed in 1% OsO_4 (2 h for tissues, 1 h for cells), dehydrated in ethanol, embedded in Epon 812 and polymerized at 70˚C for 48 h. Ultrathin sections (70 nm) were stained with 2% uranyl acetate in 50% ethanol for 15 min at room temperature in the dark, followed by lead citrate for 5 min at room temperature, and examined under a transmission electron microscope (HT7800; Hitachi, Ltd.). TEM images were analyzed using ImageJ software (version 1.53k; National Institutes of Health).

Cell culture. H9C2 cells (cat. no. ZQ0102; Zhongqiaoxinzhou Biotechnology Co., Ltd.) were cultured in 6-well plates at a density of $1x10^5$ cells/well in DMEM (Gibco; Thermo Fisher Scientific, Inc.) supplemented with 10% FBS (Gibco; Thermo Fisher Scientific, Inc.) and 1% Penicillin-Streptomycin Liquid (Beijing Solarbio Science & Technology Co., Ltd.). The cells were incubated in a CO_2 incubator with 95% air and 5% CO_2 at 37˚C.

To model myocardial OGD/R injury, H9C2 cells were cultured in a hypoxic incubator (37˚C, 94% N_2, 5% CO_2 and 1% O_2) with glucose-free and serum-free medium for 6 h. Following this, cells were cultured with fresh medium and underwent reoxygenation for 12 h in a mixed gas environment (95% air and 5% CO_2 at 37˚C). For groups treated with RMZ, reoxygenation was conducted using DMEM containing 100 μg/ml RMZ, a dosage determined based on prior literature (24). MK2206 (HY-108232, MCE) was dissolved in DMSO (10 mmol/l). For the OGD/R + RMZ + DMSO group, pretreatment was performed with DMEM containing DMSO (0.25 ml/l) and for the OGD/R + RMZ + MK2206 group, pretreatment was performed with DMEM containing 2.5 μmol/l MK2206.

Measurement of creatine kinase MB (CK-MB), lactate dehydrogenase (LDH), iron, GSH and oxidized glutathione (GSSG) contents. After treatment, tissues and cells were homogenized with PBS (G4202; Wuhan Servicebio Technology Co., Ltd.). The supernatant was collected for measuring CK-MB (cat. no. JM-03084M1, Jiangsu Jingmei Biotechnology Co., Ltd.), LDH (cat. no. C0016; Beyotime Biotechnology), iron (cat. no. E-BC-K773-M; Elabscience Bionovation Inc.), GSH (cat. no. E-BC-K030-M; Elabscience Bionovation Inc.) and GSSG (cat. no. E-BC-K097-M; Elabscience Bionovation Inc.) contents, following the instruction of the respective kits.

Dihydroethidine (DHE) staining. H9C2 cells were stained with the superoxide-sensitive dye DHE (cat. no. 104821-25-2, Beijing Solarbio Science & Technology Co., Ltd.) and incubated for 30 min at 37˚C in a humidified dark chamber. Afterwards, cells were washed three times with 1X PBS, counterstained with DAPI for 5 min at room temperature and mounted with an anti-fade mounting medium.

Hoechst 33342/PI double staining. For Hoechst 33342/PI staining, H9C2 cells grown on coverslips were treated with 5 μg/ml Hoechst 33342 (15 min) and 10 μg/ml propidium iodide (PI, 5 min) at 37˚C in accordance with the Hoechst 33342/PI Double Stain Kit (cat. no. CA1120, Beijing Solarbio Science & Technology Co., Ltd.).

Statistical analysis. Data are presented as mean ± SEM. Normality was assessed using the Shapiro-Wilk test and homogeneity of variances was evaluated with Levene's test. Multiple group comparisons were analyzed using one-way ANOVA followed by Tukey's post-hoc test. When assumptions were violated, non-parametric alternatives (Kruskal-Wallis test followed by Dunn's post-hoc test) were applied. All statistical analyses were conducted using GraphPad Prism version 8.0.2 (Dotmatics). P<0.05 was considered to indicate a statistically significant difference.

Results

RMZ alleviates I/R-induced cardiac dysfunction. To evaluate the myocardial protective effect of RMZ, serum levels of CK-MB and LDH, along with echocardiographic parameters, were measured. Myocardial ischemia-reperfusion surgery was conducted to assess the therapeutic potential of RMZ (Fig. 1A). Successful induction of I/R injury was confirmed by significant elevations in serum CK-MB and LDH levels in the I/R group compared to sham controls (Fig. 1B). Cardiac function was further assessed using M-mode echocardiography (Fig. 1C). No significant differences in EF, FS, LVESD and LVEDD were observed between the Sham and RMZ groups under baseline conditions (Fig. 1D). The I/R group demonstrated markedly impaired left ventricular systolic function, indicated by reduced EF and FS, along with enlarged ventricular dimensions, evidenced by increased LVESD and LVEDD (Fig. 1C and D). By contrast, RMZ treatment markedly attenuated these I/R-induced alterations. Compared to the I/R group, mice in the I/R + RMZ group exhibited higher EF and FS values, along with lower LVESD and LVEDD (Fig. 1C and D). Consistent with these findings, serum levels of CK-MB and LDH were notably decreased in RMZ-treated mice following I/R injury (Fig. 1B). These biochemical results closely correlate with the echocardiographic data, indicating that RMZ confers substantial cardioprotective effects in the setting of MIRI.

RMZ attenuates I/R-induced CMs histological damage and cell death. Representative myocardial tissue sections from each group are shown in Fig. 2A. Hematoxylin and eosin staining revealed extensive disorganization of left ventricular CMs in the I/R group, characterized by evident fragmentation of myocardial fibers. This structural disruption was markedly attenuated by RMZ treatment (Fig. 2A). Additionally, WGA

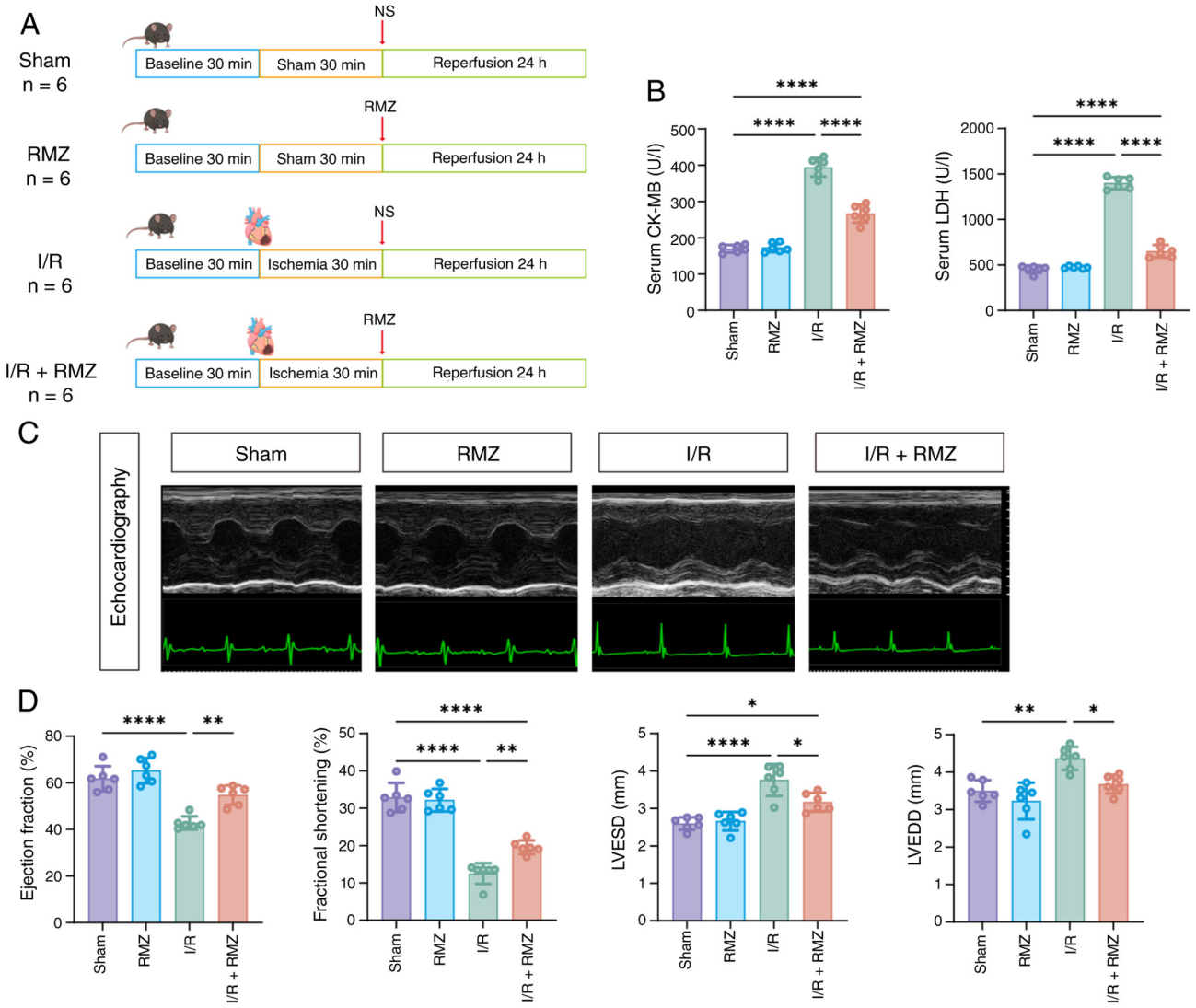

Figure 1. RMZ alleviates I/R-induced cardiac dysfunction. (A) Schematic of the experimental design. The I/R model was established by ligation of the LAD for 30 min followed by reperfusion for 24 h. RMZ (15 mg/kg) or NS was administered before reperfusion. (B) Serum CK-MB and LDH levels in each group. (C) Representative echocardiographic images of hearts from each group. (D) Quantitative analysis of left ventricular EF, left ventricular FS, LVEDD and LVESD determined by echocardiography. Data are presented as mean ± SEM, n=6 mice; *P<0.05, **P<0.01, and ****P<0.0001. RMZ, Remimazolam; I/R, ischemia and reperfusion; LAD, left anterior descending coronary artery; NS, normal saline; CK-MB, MB form of creatine kinase; LDH, lactate dehydrogenase; EF, ejection fraction FS, fractional shortening; LVEDD, left ventricular end-diastolic dimension; LVESD, left ventricular end-systolic dimension.

staining of the CM membrane demonstrated structural damage, blurred cellular boundaries and reduced cell size in the I/R group (Fig. 2A). RMZ administration markedly ameliorated these MIRI-induced abnormalities and increased CM size (Fig. 2B). Furthermore, the I/R + RMZ group exhibited a reduction in the number of TUNEL-positive nuclei compared to the I/R group (Fig. 2C and D).

Transcriptomic analysis highlights the negative role of ferroptosis in MIRI. To obtain initial exploratory evidence regarding the potential involvement of ferroptosis in MIRI, the publicly available dataset GSE141512 was analyzed, which comprises peripheral blood mononuclear cells transcriptomic profiles from six control subjects and six patients with acute MI. This dataset served as an initial screening tool to identify ferroptosis-related transcriptional signatures associated with MI. Applying screening thresholds of $|\log_2 FC| \geq 0.5$ and FDR <0.05, a total of 870 upregulated and 1,440 downregulated genes were identified in the peripheral blood mononuclear cell samples from patients with MI. A $|\log_2 FC|$ threshold of 0.5 was selected to capture biologically meaningful variations while maintaining sensitivity to subtle transcriptional alterations. All DEGs are represented in the volcano plot (Fig. 3A). An intersection analysis between the identified DEGs and FRGs revealed 80 DEFRGs.

To explore the biological features of these DEFRGs, GO and KEGG pathway enrichment analyses were conducted (Fig. 3B and C). Within the GO category, DEFRGs exhibited significant enrichment in long-chain fatty acid import across the plasma membrane, deoxyribonuclease activity, lipoxygenase activity and 1-phosphatidylinositol-3-kinase (PI3K) activity (Fig. 3B). KEGG pathway analysis identified significant enrichments in pathways including ferroptosis, apoptosis and necroptosis (Fig. 3C). Furthermore, GSEA revealed a significant positive enrichment of DEFRGs in the ferroptosis pathway (NES=1.68; FDR <0.05; Fig. 3D).

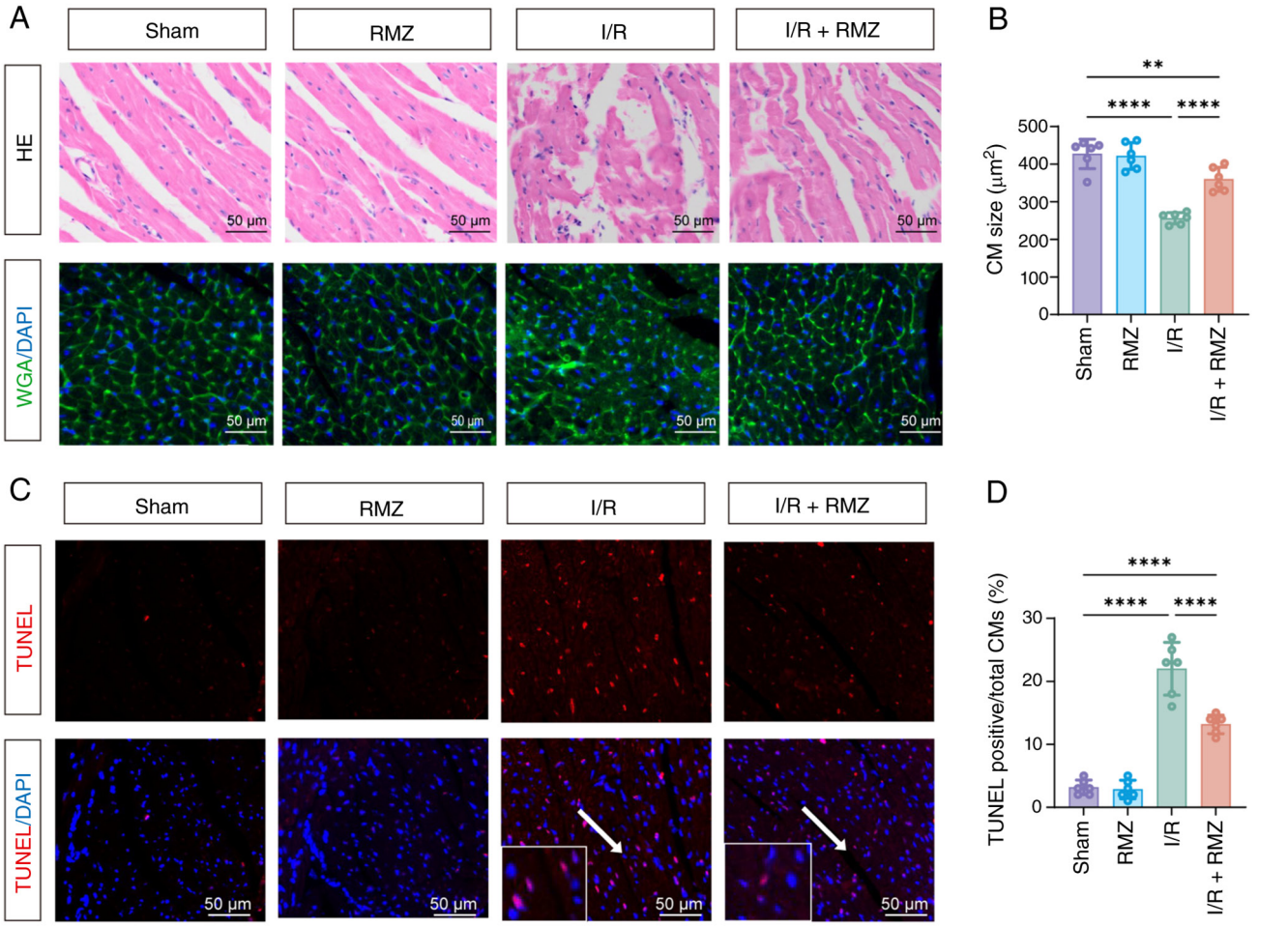

Figure 2. RMZ alleviates I/R-induced CM histological damage. (A) HE staining of heart tissues and WGA (green) staining to assess CM cross-sectional area. (B) Quantitative analysis of CM cross-sectional size. (C) TUNEL staining of heart tissues. (D) Quantitative analysis of TUNEL-positive cells. Data are presented as mean ± SEM, n=6 mice. Statistical significance was determined as follows: **P<0.01, and ****P<0.0001. RMZ, Remimazolam; I/R, ischemia and reperfusion; HE, hematoxylin and eosin; WGA, Wheat Germ Agglutinin; CMs, cardiomyocytes.

Subsequently, the dataset GSE160516 was analyzed to obtain transcriptomic data from myocardial tissue, complementing the aforementioned human blood-based analysis. This dataset, obtained from the GEO database, comprises transcriptomic profiles from heart tissues of four sham mice and four MIRI mice. A total of 2,799 upregulated and 2,566 downregulated genes were identified in MIRI tissues (Fig. 3E), including 198 DEFRGs. Within the GO category, DEFRGs exhibited significant enrichment in the inflammatory response and long-chain fatty acid import across the plasma membrane (Fig. 3F). KEGG pathway analysis revealed significant enrichments in pathways including ferroptosis, fatty acid biosynthesis and metabolism (Fig. 3G). Similarly, GSEA indicated significant positive enrichment of DEFRGs in the ferroptosis pathway (NES=1.1; FDR <0.05; Fig. 3H). These transcriptomic findings provide preliminary evidence supporting an association between ferroptosis and MIRI.

RMZ protects against I/R-induced cardiac injury by inhibiting ferroptosis in mice. To further investigate the impact of RMZ on ferroptosis during MIRI, the ferroptosis inhibitor Fer-1 was employed as a positive control (Fig. 4A). The cardioprotective effects of RMZ against I/R-induced myocardial injury were first evaluated. I/R-induced cardiac injury resulted in significant myocardial damage, evidenced by markedly elevated serum CK-MB and LDH levels (Fig. 4B and C). Hematoxylin and eosin staining revealed that the Sham group exhibited regularly arranged cardiomyocytes with intact myofibrillar architecture and no obvious pathological changes (Fig. 4D and E). In the I/R group, the ischemic zone displayed severe myofibrillar disarray, extensive disruption, dissolution and patchy pallor, with a notably increased infarct area, indicating profound myocardial structural damage induced by MIRI (Fig. 4D and E). Fer-1 treatment markedly attenuated these ischemic alterations, leading to reduced myofibrillar disruption, improved alignment and a marked decrease in infarct area (Fig. 4D and E). Similarly, RMZ administration alleviated I/R-induced myocardial injury, with reduced pallor area, diminished myofibrillar disruption and dissolution, improved myofibrillar alignment and a markedly reduced infarct area compared to the I/R group (Fig. 4D and E).

TEM further confirmed the protective effects of RMZ on myocardial ultrastructure. In the Sham group, mitochondria were regularly arranged, with intact membranes and well-defined cristae (Fig. 4F). By contrast, the I/R group exhibited disorganized mitochondrial arrangement, with some mitochondria showing swelling, degeneration, disrupted cristae and partial dissolution of the outer membrane, while others

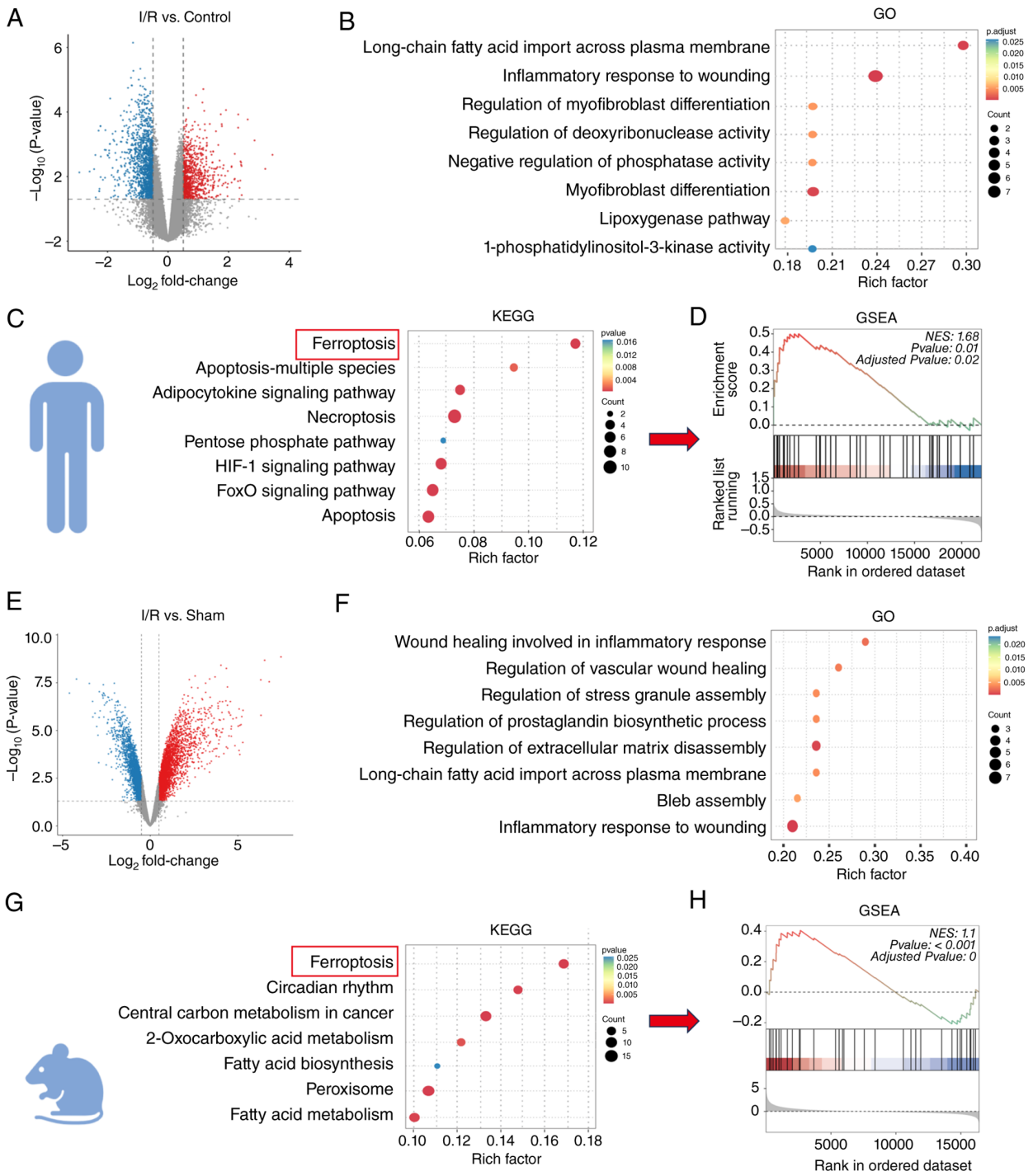

Figure 3. Transcriptomic analysis reveals the negative role of ferroptosis in MIRI. (A) Volcano plot of differentially expressed genes in peripheral blood mononuclear cells from patients with MI vs. controls (GSE141512). (B) GO enrichment analysis of DEFRGs in GSE141512. (C) KEGG enrichment analysis of DEFRGs in GSE141512. (D) GSEA confirmed positive enrichment of DEFRGs in the ferroptosis pathway in GSE141512 (NES=1.68, FDR <0.05). (E) Volcano plot of mouse GSE160516. (F) GO enrichment analysis of DEFRGs in GSE160516. (G) KEGG enrichment analysis of DEFRGs in GSE160516. (H) GSEA confirmed positive enrichment of DEFRGs in the ferroptosis pathway in GSE160516 (NES=1.1, FDR <0.05). MIRI, myocardial ischemia reperfusion injury; MI, myocardial infarction; DEFRGs, differentially expressed ferroptosis-related genes; NES, normalized enrichment score; FDR, false discovery rate; GO, Gene Ontology; KEGG, Kyoto Encyclopedia of Genes and Genomes; GSEA, Gene Set Enrichment Analysis; I/R, ischemia and reperfusion.

appeared shrunken and electron-dense (Fig. 4F). Fer-1 treatment markedly mitigated mitochondrial damage, with relatively intact membranes and improved cristae structure compared to the I/R group (Fig. 4F). RMZ administration also markedly protected mitochondrial ultrastructure (Fig. 4F). These findings indicate that RMZ, akin to the ferroptosis inhibitor Fer-1, exerts potent cardioprotective effects against MIRI.

Next, the association between the cardioprotective effect of RMZ and ferroptosis inhibition was examined. I/R injury triggered ferroptosis, as evidenced by a marked reduction in GSH content, a decreased GSH/GSSG ratio and significant Fe^{2+} accumulation (Fig. 4G). Furthermore, I/R injury led to increased lipid peroxidation, indicated by downregulated GPX4 protein expression (Fig. 4H and I) and elevated 4-HNE

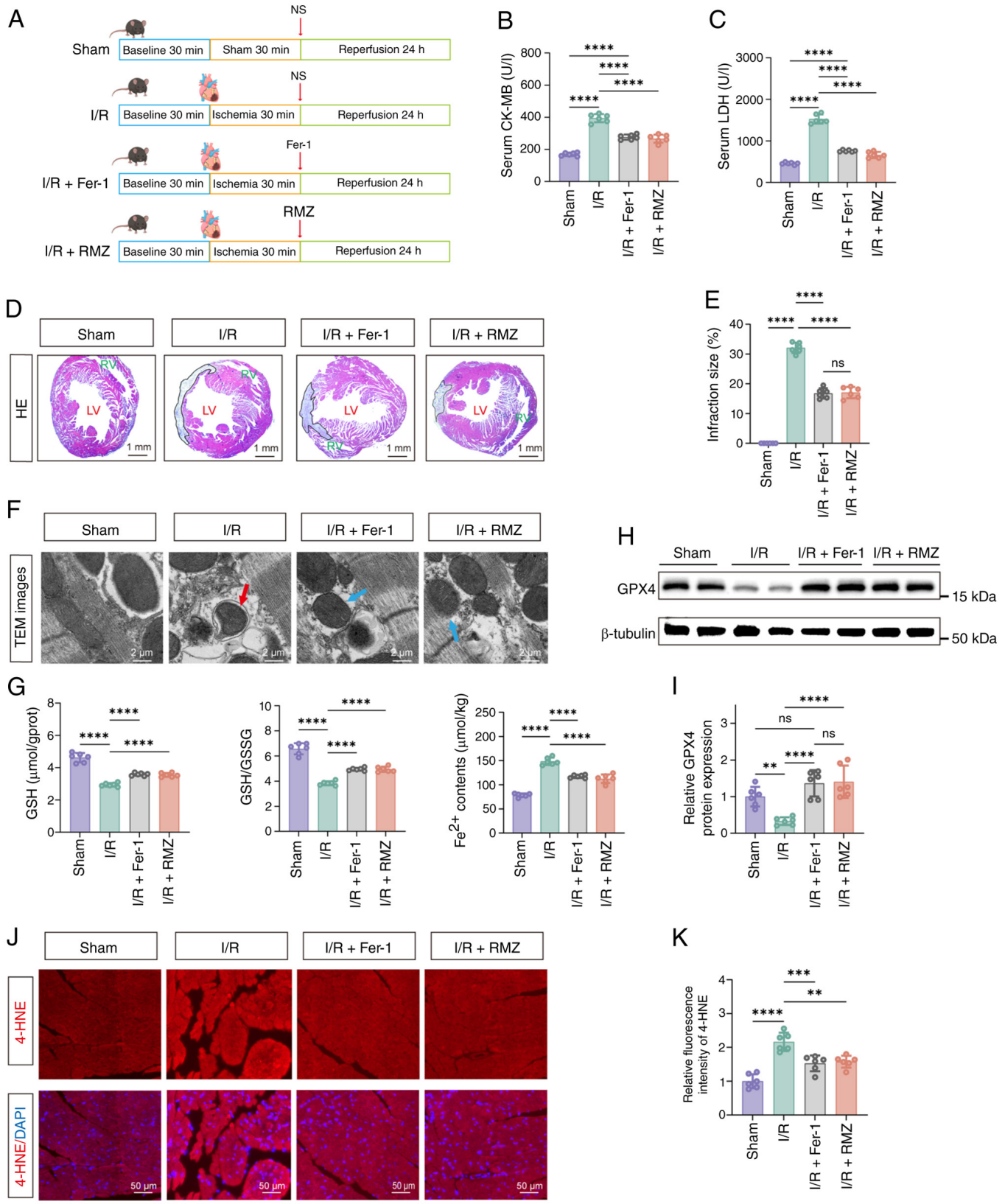

Figure 4. RMZ inhibits I/R-induced ferroptosis *in vivo*. (A) Schematic of the experimental design. The I/R model was established by ligation of the LAD for 30 min followed by reperfusion for 24 h. Fer-1 (1 mg/kg), RMZ (15 mg/kg), or NS was administered before reperfusion. (B) Serum CK-MB and (C) LDH levels in each group. (D) Representative HE staining of heart tissues from each group (scale bar, 1 mm). The infarcted area is marked by the solid line. (E) Quantitative analysis of infarct area. (F) Transmission electron microscopy of myocardial tissues from mice in different groups. Red arrows indicate swollen mitochondria with disrupted cristae and outer membrane dissolution. Blue arrows indicate relatively preserved mitochondria with mild cristae disruption (scale bar, 2 μm). (G) GSH, GSH/GSSG and Fe^{2+} levels in heart tissues. (H) Western blotting images of GPX4 and β-Tubulin. (I) Quantitative analysis of GPX4 protein expression. (J) 4-HNE staining of heart tissues. (K) Quantitative analysis of 4-HNE fluorescence intensity. Data are presented as mean ± SEM, n=6 mice. **P<0.01, ***P<0.001 and ****P<0.0001. RMZ, Remimazolam; I/R, ischemia and reperfusion; LAD, left anterior descending coronary artery; Fer-1, Ferrostatin-1; NS, normal saline; CK-MB, MB form of creatine kinase; LDH, lactate dehydrogenase; HE, hematoxylin and eosin; GSH, glutathione; GSSG, oxidized GSH; GPX4; glutathione peroxidase 4; TEM, transmission electron microscopy.

fluorescence intensity (Fig. 4J and K). Both Fer-1 and RMZ interventions effectively reversed these ferroptotic hallmarks, demonstrating that RMZ alleviates MIRI by inhibiting ferroptosis, restoring antioxidant capacity and preserving GPX4-mediated lipid peroxide clearance.

The protective effect of RMZ against OGD/R-induced injury in H9C2 cells is mediated by p-AKT. AKT plays a critical role in regulating ferroptosis, as its activation inhibits proteins and pathways associated with ferroptosis, promoting cell survival (28). AKT inhibitors mitigate the cardioprotective and anti-ferroptotic effects against cardiotoxicity marked by ferroptosis (29). Building on transcriptomic evidence indicating altered PI3K activity (Fig. 3B), corresponding protein changes were assessed. In the present study, western blotting results revealed a significant reduction in p-AKT (Ser473) expression following I/R intervention, while RMZ administration led to an upregulation of p-AKT expression (Fig. 5A-E). Thus, p-AKT activation may mediate the anti-ferroptosis effect of RMZ in the context of I/R.

To investigate the underlying mechanism further, an *in vitro* OGD/R model was established using H9C2 cells (Fig. 5F). In alignment with the *in vivo* findings, OGD/R conditions resulted in a significant increase in the PI-positive rate, indicating enhanced cell death (Fig. 5G and H). RMZ treatment notably reversed this effect, suggesting protective actions of RMZ against OGD/R-induced injury (Fig. 5G and H). To determine whether p-AKT mediates the anti-injury effects of RMZ, MK2206, a well-established AKT inhibitor, was used to suppress p-AKT expression. The inhibition of AKT phosphorylation negated the protective effects of RMZ, evidenced by the reversal in the PI-positive rate (Fig. 5G and H). These results implied that p-AKT participates functionally in the cytoprotective pathway activated by RMZ. The effect of AKT activation on SLC7A11 and GPX4 is context-dependent; in sham hearts, RMZ did not further elevate SLC7A11 or GPX4 expression. Under I/R injury, however, oxidative stress depletes these proteins and RMZ-mediated AKT activation counteracts this depletion, thereby restoring their expression (Fig. 5A-E). Consequently, p-AKT activation may mediate RMZ's anti-ferroptosis effect during I/R.

RMZ alleviates OGD/R-induced ferroptosis in H9C2 cells. To assess RMZ's effect on OGD/R-induced ferroptosis in H9C2 cells, ROS levels were measured using DHE staining, while intracellular Fe^{2+}, GSH and GSSG levels were quantified through colorimetric assays (Fig. 6). ROS accumulation in H9C2 cells was quantified based on DHE fluorescence intensity (Fig. 6A). Results demonstrated that RMZ markedly attenuated OGD/R-induced ROS accumulation, indicating suppression of ferroptosis (Fig. 6A and B). However, this protective effect was largely abolished by inhibiting AKT phosphorylation, which markedly increased ROS fluorescence intensity compared to the OGD/R + RMZ group (Fig. 6A and B).

Consistent with the ROS data, examination of the myocardial GSH antioxidant system revealed that OGD/R injury decreased GSH levels, elevated GSSG levels and reduced the GSH/GSSG ratio, alongside increased intracellular Fe^{2+} levels, indicating enhanced oxidative stress and diminished antioxidant capacity with disrupted iron homeostasis (Fig. 6C-G). RMZ treatment effectively reversed these alterations, elevating GSH, reducing GSSG, restoring the GSH/GSSG ratio and decreasing Fe^{2+} accumulation, thus supporting antioxidant capacity and mitigating ferroptosis (Fig. 6C-G). Notably, inhibiting AKT phosphorylation counteracted these beneficial effects, resulting in a lower GSH/GSSG ratio and elevated Fe^{2+} levels compared to the RMZ group (Fig. 6C-G). These findings suggested that p-AKT is essential for RMZ-mediated protection against OGD/R-induced ferroptosis in H9C2 cells.

The protective effect of RMZ against OGD/R-induced ferroptosis involves the AKT/SLC7A11/GPX4 axis. To further elucidate the underlying mechanism, it is proposed that RMZ confers cardioprotection by attenuating ferroptosis, specifically through the upregulation of the AKT/SLC7A11/GPX4 axis. To test this hypothesis, the expression of key regulators involved in ferroptosis, including p-AKT, AKT, SLC7A11, GPX4 and PCNA, was examined (Fig. 7). Results indicated that OGD/R treatment markedly reduced the protein levels of p-AKT, SLC7A11, GPX4 and PCNA, all of which were markedly restored by RMZ treatment (Fig. 7A-H). Furthermore, MK2206 administration markedly counteracted the RMZ-mediated anti-ferroptotic effect, inhibiting the elevation of p-AKT along with the upregulation of SLC7A11 and GPX4 expression (Fig. 7A-H). These findings suggested that SLC7A11 and GPX4 function downstream of p-AKT in the anti-ferroptotic action of RMZ. Given that ferroptosis impairs DNA repair capacity, PCNA expression, assessed as an indicator of cellular resilience, was restored by RMZ in an AKT-dependent manner in OGD/R-treated H9C2 cells. These findings suggested that RMZ exerts anti-ferroptosis effects associated with the AKT/SLC7A11/GPX4 axis (Fig. 8).

Discussion

The present study provided compelling evidence that RMZ confers cardioprotective effects against MIRI by targeting ferroptosis, a regulated cell death pathway characterized by iron-dependent lipid peroxidation. *In vivo* experiments demonstrated that RMZ administration markedly improved I/R-induced contractile dysfunction, as evidenced by enhanced left ventricular EF and FS, while histological analysis confirmed reduced fragmentation of myocardial fibers and infarct size. These findings were corroborated by *in vitro* studies using H9C2 cells subjected to OGD/R, where RMZ inhibited ferroptotic hallmarks, including lipid peroxidation accumulation, Fe^{2+} overload and ROS bursts. These results indicated RMZ as a novel ferroptosis regulator with potential therapeutic utility in MIRI.

Mechanistically, the AKT/SLC7A11/GPX4 axis serves as a mediator of RMZ's anti-ferroptotic effects. This evidence originated from transcriptomic analysis, revealing significant enrichment in PI3K-AKT signaling and ferroptosis-related pathways. Subsequent validation of this pathway at the protein level demonstrated that RMZ treatment reversing I/R-induced suppression of this axis and RMZ upregulated p-AKT in both *in vivo* and *in vitro* models, concomitant with increased expression of SLC7A11 (a cystine-glutamate antiporter) and GPX4 (a selenoprotein peroxidase that neutralizes lipid peroxides). Notably, pharmacological inhibition of AKT phosphorylation

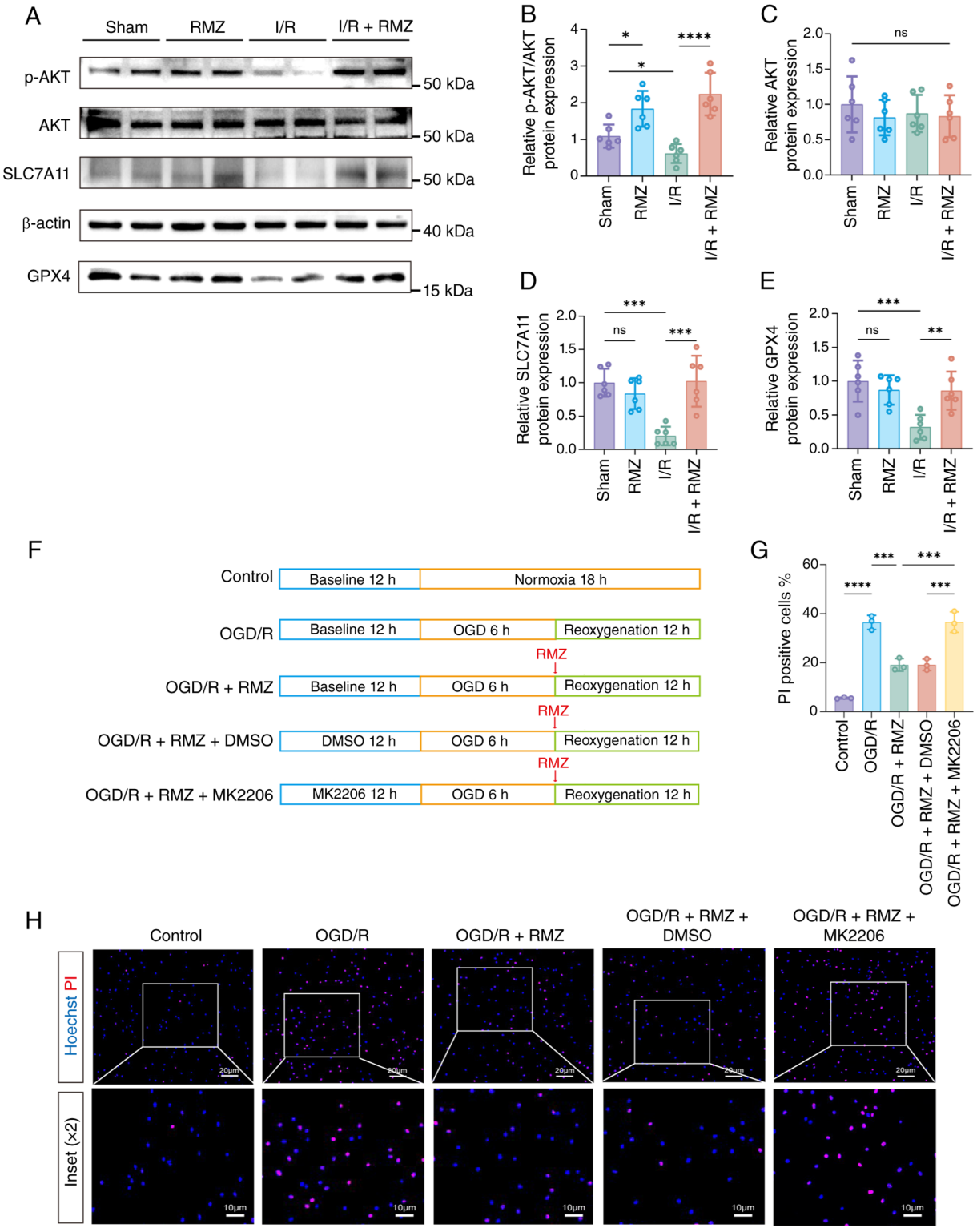

Figure 5. RMZ attenuates OGD/R-induced injury in H9C2 cells. (A) Western blotting images of p-AKT, AKT, SLC7A11, GPX4 and β-actin in mouse heart tissues. Quantitative analysis of (B) p-AKT/AKT, (C) AKT, (D) SLC7A11 and (E) GPX4 protein expression. (F) Experimental protocol using cultured H9C2 cells. (G) Quantitative analysis of PI-positive cells. (H) Effects of RMZ on cell viability were evaluated using PI staining. Data are presented as mean ± SEM, n=3 independent experiments per condition. Statistical significance was determined as follows: *P<0.05, **P<0.01, ***P<0.001 and ****P<0.0001. RMZ, Remimazolam; OGD/R, oxygen-glucose deprivation/reoxygenation; p-, phosphorylated; SLC7A11, solute carrier family 7 member 11; GPX4; glutathione peroxidase 4; PI, propidium iodide.

abolished RMZ-induced upregulation of SLC7A11 and GPX4, reduced GSH levels and reversed Fe^{2+} accumulation. These findings indicated that SLC7A11 and GPX4 operate downstream of p-AKT, linking survival signaling to ferroptosis resistance.

Notably, the regulation of SLC7A11 and GPX4 by RMZ exhibited a clear context dependence. Under sham conditions, RMZ did not further elevate SLC7A11 or GPX4 protein levels beyond baseline, despite increasing p-AKT. By contrast, during I/R injury RMZ restored their expression toward sham levels

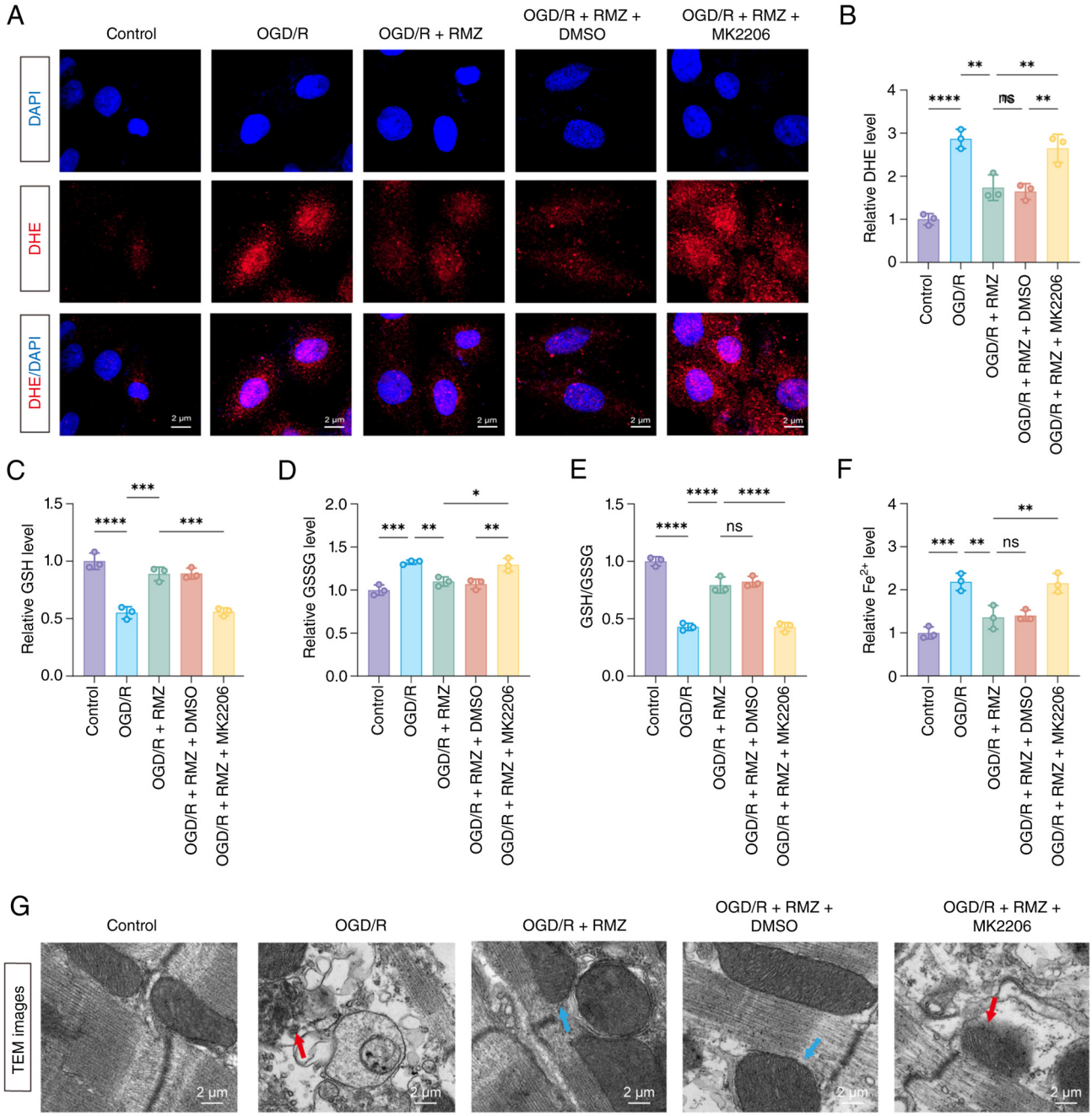

Figure 6. The protective effect of RMZ against OGD/R-induced ferroptosis is mediated by p-AKT. (A) ROS accumulation in H9C2 cells was quantified based on DHE staining. (B) Quantitative analysis of DHE fluorescence intensity. Relative levels of cellular (C) GSH, (D) GSSG, (E) GSH/GSSG and (F) Fe^{2+} in cells. (G) Transmission electron microscopy of cells from different groups. Red arrows indicate swollen mitochondria with disrupted cristae and outer membrane dissolution. Blue arrows indicate relatively preserved mitochondria with mild cristae disruption. Data are presented as mean ± SEM, n=3 independent experiments per condition. Statistical significance was determined as follows: *P<0.05, **P<0.01, ***P<0.001 and ****P<0.0001. RMZ, Remimazolam; OGD/R, oxygen-glucose deprivation/reoxygenation; p-, phosphorylated; ROS, reactive oxygen species; DHE, dihydroethidium; GSH, glutathione; GSSG, oxidized GSH; Fe^{2+}, ferrous ion; GPX4; glutathione peroxidase 4; TEM, transmission electron microscopy; SLC7A11, solute carrier family 7 member 11.

in an AKT-dependent manner. This context-dependent pattern aligns with the established concept that AKT functions as a signaling hub, where downstream outputs are shaped by cellular stress status (30). Prior studies similarly report that AKT activation can exert divergent effects on ferroptosis-related targets depending on the presence or absence of pathological stress (31,32). While the present data did not directly define the molecular mechanisms underlying this restoration, in other systems AKT has been shown to promote ferroptosis resistance via downstream pathways such as NRF2 activation or modulation of protein turnover (31,32). However, whether these mechanisms actually contribute to the restoration of SLC7A11 and GPX4 in the I/R + RMZ group remains to be determined and direct experimental testing is warranted in future studies. In addition to these anti-ferroptotic effects, RMZ also restored PCNA expression in an AKT-dependent manner in OGD/R-treated H9C2 cells. In post-mitotic cardiomyocytes, PCNA upregulation does not signify proliferation but rather reflects enhanced DNA repair capacity and cellular resilience in response to stress. During I/R injury, oxidative DNA damage

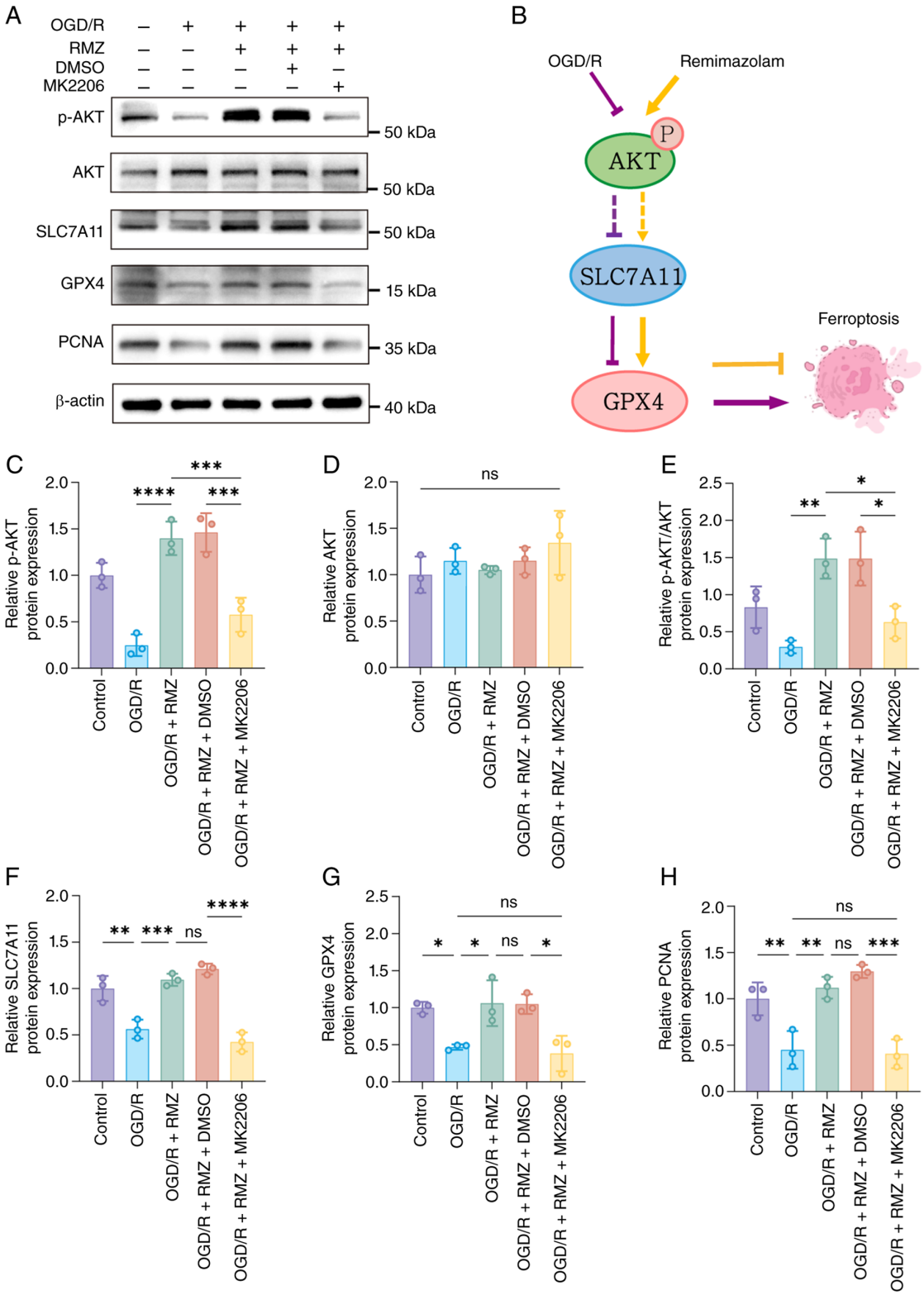

Figure 7. RMZ alleviates OGD/R-induced ferroptosis in H9C2 cells involves the AKT/SLC7A11/GPX4 axis. (A) Western blotting image of the AKT/SLC7A11/GPX4 axis. (B) Flowchart of the underlying pathway mechanism. Quantitative analysis of (C) p-AKT, (D) AKT, (E) p-AKT/AKT, (F) SLC7A11, (G) GPX4 and (H) PCNA protein expression levels in H9C2 cells. Data are presented as mean ± SEM, n=3 independent experiments per condition. *P<0.05, **P<0.01, ***P<0.001 and ****P<0.0001. RMZ, Remimazolam; OGD/R, oxygen-glucose deprivation/reoxygenation; AKT, Protein Kinase B; SLC7A11, solute carrier family 7 member 11; GPX4; glutathione peroxidase 4; p-, phosphorylated; PCNA, proliferating cell nuclear antigen.

accumulates and impaired DNA repair exacerbates cardiomyocyte dysfunction and death (33). Thus, RMZ-induced restoration of PCNA expression likely contributes to promoting recovery of injured cardiomyocytes, which may synergize with the anti-ferroptotic pathway to promote cardiomyocyte survival and functional recovery following I/R injury.

The findings of the present study align with and extend previous reports. Prior studies linked RMZ to AKT activation

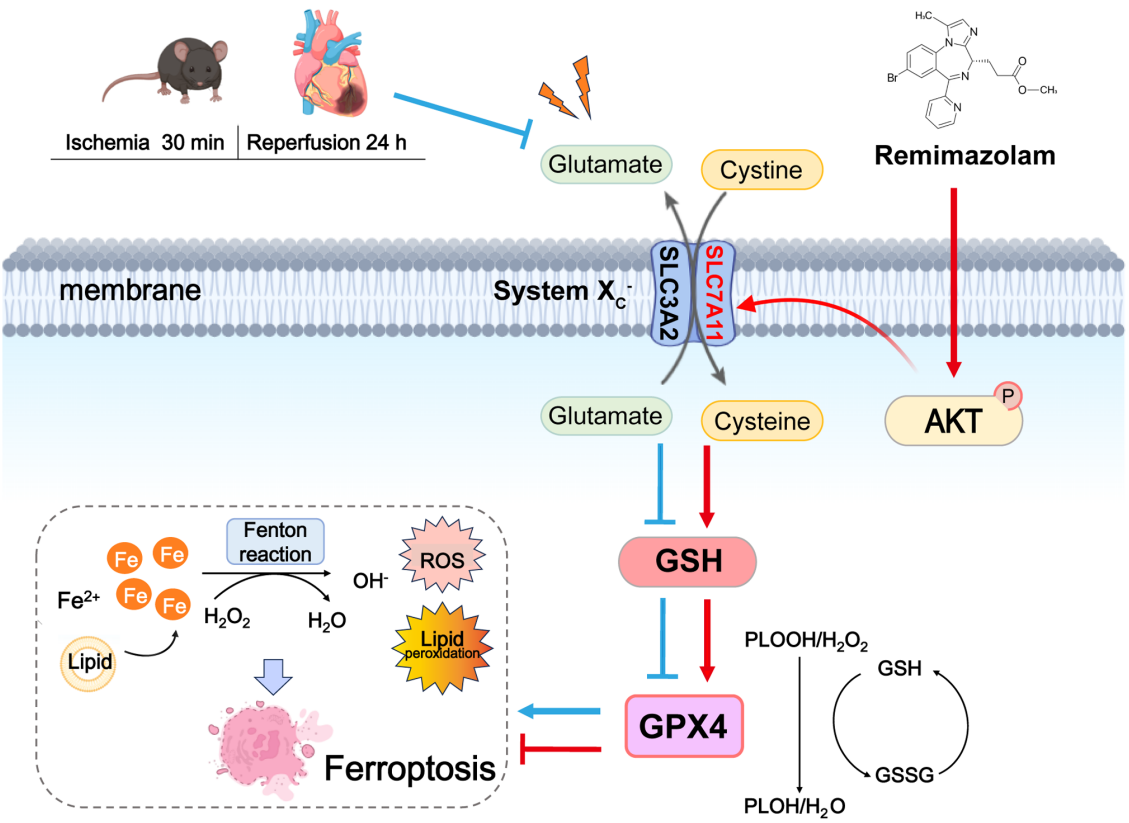

Figure 8. Remimazolam mitigates MIRI by inhibiting ferroptosis involving the AKT/SLC7A11/GPX4 signaling pathway. This schematic represents a working hypothesis based on the current findings. MIRI, myocardial ischemia reperfusion injury; SLC7A11, solute carrier family 7 member 11; SLC3A2, solute carrier family 2 member 2; GPX4; glutathione peroxidase 4; ROS, reactive oxygen species; GSH, glutathione; p, phosphorylation GSSG, oxidized GSH.

in cerebral I/R (21) and acute lung injury (34), suggesting that AKT modulation may represent a common mechanism underlying RMZ's protective effects across multiple organ systems. However, the present study demonstrated that RMZ-induced AKT activation is associated with the SLC7A11/GPX4 signaling to inhibit ferroptosis. This ferroptosis mechanism adds a new dimension to the understanding of RMZ's pharmacological actions.

The anti-ferroptotic properties of RMZ expand its established pharmacological profile beyond sedative-hypnotic effects. As an ultra-short-acting benzodiazepine, RMZ is widely used in clinical practice for procedural sedation and general anesthesia due to its rapid onset, esterase-dependent metabolism and minimal hemodynamic impact (35-38). Emerging evidence suggests pleiotropic organ-protective effects: in cardiac surgery, RMZ combined with esketamine reduces perioperative myocardial injury biomarkers (39,40), while in neurocritical care, it improves neurological outcomes in patients with ischemic stroke (22,41). Preclinical studies have linked RMZ to the inhibition of oxidative stress (via AKT/GSK-3β/NRF2 in cerebral I/R) (21) and apoptosis (via FOXO1/3 in hepatic I/R) (20). The findings presented in the present study add a new dimension to this protective repertoire, demonstrating that RMZ modulates ferroptosis, a pathway not previously associated with benzodiazepine pharmacology.

The role of ferroptosis in MIRI pathogenesis is increasingly recognized, rendering the targeting of this pathway a promising therapeutic strategy. Therapeutic options involving anti-ferroptotic compounds for cardiovascular diseases include deferoxamine, Fer-1 and liproxstatin-1 (Lip-1). Lip-1 and Fer-1 can both reduce infarct size by preserving GPX4 activity and inhibiting lipid peroxidation (42,43). Similarly, iron chelators such as deferoxamine mitigate MIRI by limiting labile iron availability (44,45). However, the main disadvantage of Lip-1 and Fer-1 is their poor solubility in water, complicating intravenous administration in acute pathologies such as AMI, takotsubo syndrome and sepsis. Water-soluble ferroptosis inhibitors similar to Lip-1 and Fer-1 are thus needed.

The present study presented a clinically promising option to address these shortcomings, demonstrating that RMZ reduces Fe^{2+} accumulation and lipid ROS production in MIRI models. Intraperitoneal administration immediately before reperfusion was selected to mimic the clinically relevant timing of RMZ administration in patients undergoing primary PCI, cardiac surgery, or procedural sedation in catheterization laboratories. Its rapid onset (1-3 min) and favorable hemodynamic profile further reinforce the clinical relevance of this administration regimen. Notably, Li *et al* (46) recently demonstrated that RMZ improves neurological function in a murine model of intracerebral hemorrhage by suppressing ferroptosis, suggesting that anti-ferroptotic effects may represent a conserved mechanism of RMZ's organ protection across different tissues. This consistency across systems enhances the translational potential of these findings. For patients experiencing MI, maintaining stable blood pressure is crucial. The primary advantage of RMZ in patients with cardiovascular disease lies in its excellent hemodynamic stability (47). Compared with propofol, a commonly used clinical sedative,

RMZ is associated with a markedly lower risk of hypotension. Additionally, the incidence and severity of respiratory depression caused by RMZ are considered lower than those associated with propofol (47). While these characteristics suggest potential roles for RMZ during the clinical timeline of MI (pre-hospital or catheterization use), direct extrapolation is speculative due to differences in administration route, timing and patient populations between the experimental model and clinical practice. Thus, this proposal serves as a working hypothesis that requires validation in large-animal models and clinical trials, with long-term outcomes needing further investigation.

Despite these advances, several limitations warrant consideration. First, the upstream molecular target through which RMZ activates AKT remains unidentified. While RMZ, as a benzodiazepine, typically acts via GABA_A receptors, it remains unclear whether this interaction plays a role in AKT phosphorylation and requires further investigation. Unbiased methodologies, such as chemical proteomics or affinity purification, could help identify direct RMZ-binding proteins. Second, the study focused on acute MIRI endpoints at 24 h post-reperfusion. Future research should evaluate long-term outcomes, including cardiac remodeling and survival, using large-animal models (such as swine with coronary artery occlusion) to more closely mimic clinical conditions. Third, the potential involvement of additional pathways, such as Nrf2-mediated antioxidant responses or AMPK-dependent mitochondrial protection, cannot be excluded, as they may synergize with the AKT/SLC7A11/GPX4 axis to enhance RMZ's cardioprotective effects. Multi-omics integration and CRISPR screening could aid in mapping the comprehensive spectrum of RMZ's molecular targets in MIRI. Fourth, although the RMZ concentrations and doses used in the present study were based on existing literature, conducting a systematic dose-response experiment would further substantiate its concentration-dependent cardioprotective effects. Finally, the use of H9C2 cells instead of primary cardiomyocytes limits translational implications; validation in primary or hiPSC-derived cells would enhance the relevance of the findings.

In conclusion, the present study is the first, to the best of the authors' knowledge, to demonstrate that RMZ attenuates MIRI by inhibiting ferroptosis, primarily involving the activation of the AKT/SLC7A11/GPX4 axis. This discovery not only deepens the understanding of the regulatory network governing ferroptosis but also offers a novel clinical therapeutic option for the combination therapy of MIRI.

Acknowledgements

Not applicable.

Funding

The present study was supported by grants from the Hunan Provincial Natural Science Foundation of China (grant nos. 2024JJ5243, 2025JJ81005 and 2026JJ82381), the Hunan Cancer Hospital Climb Plan (grant no. 2023NSFC-A005) and the Wu Jieping Medical Foundation (grant no. 320.6750.2025-5-54).

Availability of data and materials

The data generated in the present study may be requested from the corresponding author.

Authors' contributions

XY-C and XT-H carried out most of the *in vitro* and *in vivo* experiments. YQ-Z, JW and CJ contributed to experimental designs and revised the manuscript. JX, YY, JH-Z and XY-C conceived the study, supervised the work and revised the manuscript. All authors discussed the data and commented on the manuscript. XY-C, JX and YY confirm the authenticity of all the raw data. All authors read and approved the final manuscript.

Ethics approval and consent to participate

The present study was authorized by the Animal Studies Ethics Committee of Hunan cancer hospital (approval no. 2025-410) and was implemented in accordance with the Guide for the Care and Use of Laboratory Animals.

Patient consent for publication

Not applicable.

Competing interests

The authors declare that they have no competing interests.

References

1. GBD 2016 Causes of Death Collaborators: Global, regional, and national age-sex specific mortality for 264 causes of death, 1980-2016: A systematic analysis for the global burden of disease study 2016. Lancet 390: 1151-1210, 2017.
2. Heusch G: Myocardial ischaemia-reperfusion injury and cardioprotection in perspective. Nat Rev Cardiol 17: 773-789, 2020.
3. Du B, Fu Q, Yang Q, Yang Y, Li R, Yang X, Yang Q, Li S, Tian J and Liu H: Different types of cell death and their interactions in myocardial ischemia-reperfusion injury. Cell Death Discov 11: 87, 2025.
4. Xiang Q, Yi X, Zhu XH, Wei X and Jiang DS: Regulated cell death in myocardial ischemia-reperfusion injury. Trends Endocrinol Metab 35: 219-234, 2024.
5. Dixon SJ, Lemberg KM, Lamprecht MR, Skouta R, Zaitsev EM, Gleason CE, Patel DN, Bauer AJ, Cantley AM, Yang WS, *et al*: Ferroptosis: An iron-dependent form of nonapoptotic cell death. Cell 149: 1060-1072, 2012.
6. Tang D, Chen X, Kang R and Kroemer G: Ferroptosis: Molecular mechanisms and health implications. Cell Res 31: 107-125, 2021.
7. Masaldan S, Bush AI, Devos D, Rolland AS and Moreau C: Striking while the iron is hot: Iron metabolism and ferroptosis in neurodegeneration. Free Radic Biol Med 133: 221-233, 2019.
8. Zhou Y, Lin W, Rao T, Zheng J, Zhang T, Zhang M and Lin ZL: Ferroptosis and its potential role in the nervous system diseases. J Inflamm Res 15: 1555-1574, 2022.
9. Chen F, Kang R, Tang D and Liu J: Ferroptosis: Principles and significance in health and disease. J Hematol Oncol 17: 41, 2024.
10. Wang Y, Wu S, Li Q, Sun H and Wang H: Pharmacological inhibition of ferroptosis as a therapeutic target for neurodegenerative diseases and strokes. Adv Sci (Weinh) 10: e2300325, 2023.
11. Gao X, Hu W, Qian D, Bai X, He H, Li L and Sun S: The mechanisms of ferroptosis under hypoxia. Cell Mol Neurobiol 43: 3329-3341, 2023.
12. Kilpatrick GJ, Mcintyre MS, Cox RF, Stafford JA, Pacofsky GJ, Lovell GG, Wiard RP, Feldman PL, Collins H, Waszczak BL and Tilbrook GS: CNS 7056: A novel ultra-short-acting benzodiazepine. Anesthesiology 107: 60-66, 2007.

13. Rogers WK and McDowell TS: Remimazolam, a short-acting GABA(A) receptor agonist for intravenous sedation and/or anesthesia in day-case surgical and non-surgical procedures. IDrugs 13: 929-937, 2010.
14. Song X, Wang F, Dong R, Zhu K and Wang C: Efficacy and safety of remimazolam tosilate combined with esketamine for analgesic sedation in mechanically ventilated ICU patients: A single-arm clinical study protocol. Front Med (Lausanne) 9: 832105, 2022.
15. Tanious MK, Beutler SS, Kaye AD and Urman RD: New hypnotic drug development and pharmacologic considerations for clinical anesthesia. Anesthesiol Clin 35: e95-e113, 2017.
16. Goudra B, Gouda G and Mohinder P: Recent developments in drugs for GI endoscopy sedation. Dig Dis Sci 65: 2781-2788, 2020.
17. Sneyd JR: Remimazolam-current status, opportunities and challenges. Anesthesiol Perioper Sci 1: 25, 2023.
18. Hansen TG and Engelhardt T: Remimazolam in children: A comprehensive narrative review. Anesthesiol Perioper Sci 3: 7, 2025.
19. Liu T, Qin L, Su M, Wei Y, Yu H, Wei H, Xie Y and Chen J: Remimazolam and propofol combination in ischemic cerebrovascular disease endovascular treatment: A randomized study. Sci Rep 15: 21083, 2025.
20. Zhou B, Liu J, Jin L and Huang X: Remimazolam alleviates hepatic ischemia-reperfusion injury by activating FOXO1/3 signaling: Remimazolam alleviates hepatic ischemia reperfusion injury. BMC Gastroenterol 25: 283, 2025.
21. Duan M, Yu N, Liu J, Zhao Y, Zhang J, Song S and Wang S: Remimazolam suppresses oxidative stress and apoptosis in cerebral ischemiareperfusion injury by regulating AKT/GSK-3β/NRF2 pathway. Drug Des Devel Ther 19: 111-128, 2025.
22. Kim J, Lee S, Park B, Sim WS, Ahn HJ, Park MH and Jeong JS: Effect of remimazolam versus propofol anesthesia on postoperative delirium in neurovascular surgery: Study protocol for a randomized controlled, non-inferiority trial. Perioper Med (Lond) 13: 56, 2024.
23. Shi M, Chen J, Liu T, Dai W, Zhou Z, Chen L and Xie Y: Protective effects of remimazolam on cerebral ischemia/reperfusion injury in rats by inhibiting of NLRP3 inflammasome-dependent pyroptosis. Drug Des Devel Ther 16: 413-423, 2022.
24. Liu X, Shui G, Wang Y, Chen T, Zhang P, Liu L, Li C, Li T and Wang X: Remimazolam alleviates myocardial ischemia/reperfusion injury and inflammation via inhibition of the NLRP3/IL-1β pathway in mice. Int J Mol Med 55: 57, 2025.
25. Dong Y, Wu F, Liu K, Yue Y, Shen X, Qu Z, Yu S and Du W: Kindlin-2/Otub1/Slc7a11 axis improved cardiac ischemia reperfusion injury by inhibiting cardiomyocyte ferroptosis. Antioxid Redox Signal 43: 727-744, 2025.
26. Osmak G, Baulina N, Koshkin P and Favorova O: Collapsing the list of myocardial infarction-related differentially expressed genes into a diagnostic signature. J Transl Med 18: 231, 2020.
27. Sherman BT, Hao M, Qiu J, Jiao X, Baseler MW, Lane HC, Imamichi T and Chang W: DAVID: A web server for functional enrichment analysis and functional annotation of gene lists (2021 update). Nucleic Acids Res 50 W1): W216-W221, 2022.
28. Zhang GY, Gao Y, Guo XY, Wang GH and Guo CX: MiR-199a-5p promotes ferroptosis-induced cardiomyocyte death responding to oxygen-glucose deprivation/reperfusion injury via inhibiting Akt/eNOS signaling pathway. Kaohsiung J Med Sci 38: 1093-1102, 2022.
29. Liu X, Li D, Pi W, Wang B, Xu S, Yu L, Yao L, Sun Z, Jiang J and Mi Y: LCZ696 protects against doxorubicin-induced cardiotoxicity by inhibiting ferroptosis via AKT/SIRT3/SOD2 signaling pathway activation. Int Immunopharmacol 113: 109379, 2022.
30. Toker A and Marmiroli S: Signaling specificity in the Akt pathway in biology and disease. Adv Biol Regul 55: 28-38, 2014.
31. Fu C, Wu Y, Liu S, Luo C, Lu Y, Liu M, Wang L, Zhang Y and Liu X: Rehmannioside A improves cognitive impairment and alleviates ferroptosis via activating PI3K/AKT/Nrf2 and SLC7A11/GPX4 signaling pathway after ischemia. J Ethnopharmacol 289: 115021, 2022.
32. Gao N, Huang Z, Xie J, Gao S, Wang B, Feng H, Bao C, Tian H and Liu X: Cryptotanshinone alleviates cerebral ischemia reperfusion injury by regulating ferroptosis through the PI3K/AKT/Nrf2 and SLC7A11/GPX4 signaling pathway. J Ethnopharmacol 348: 119800, 2025.
33. Strzalka W and Ziemienowicz A: Proliferating cell nuclear antigen (PCNA): A key factor in DNA replication and cell cycle regulation. Ann Bot 107: 1127-1140, 2011.
34. Li R, Zhang C, Ren J, Deng G, Gao Y, Gao X, Li J, Zhang J, Xu X, Jin X, *et al*: Remimazolam inhibits apoptosis of endothelial and epithelial cells by activating the PI3K/AKT pathway in acute lung injury. Int Immunopharmacol 147: 113949, 2025.
35. Hu Q, Liu X, Wen C, Li D and Lei X: Remimazolam: An updated review of a new sedative and anaesthetic. Drug Des Devel Ther 16: 3957-3974, 2022.
36. Kim KM: Remimazolam: Pharmacological characteristics and clinical applications in anesthesiology. Anesth Pain Med (Seoul) 17: 1-11, 2022.
37. Lee A and Shirley M: Remimazolam: A review in procedural sedation. Drugs 81: 1193-1201, 2021.
38. Zhang H, Li H, Zhao S and Bao F: Remimazolam in general anesthesia: A comprehensive review of its applications and clinical efficacy. Drug Des Devel Ther 18: 3487-3498, 2024.
39. Xi L, Liu H, Tang X and Jiang Z: Effects of esketamine combined with remimazolam tosylate on hemodynamics during cardiovascular anesthesia. Clin Transl Sci 18: e70232, 2025.
40. Lee JY, Kim HT, Kim YJ, Lee JS, Park JW and Shin YD: Anesthetic management using remimazolam in a patient with atrial flutter: A case report. Am J Transl Res 14: 5754-5759, 2022.
41. Koo CH, Lee SU, Kim HG, Lee S, Bae YK, Oh AY, Jeon YT and Ryu JH: Effect of remimazolam on intraoperative hemodynamic stability in patients undergoing cerebrovascular bypass surgery: A prospective randomized controlled trial. Korean J Anesthesiol 78: 148-158, 2025.
42. Feng Y, Madungwe NB, Imam Aliagan AD, Tombo N and Bopassa JC: Liproxstatin-1 protects the mouse myocardium against ischemia/reperfusion injury by decreasing VDAC1 levels and restoring GPX4 levels. Biochem Biophys Res Commun 520: 606-611, 2019.
43. Ru Q, Li Y, Chen L, Wu Y, Min J and Wang F: Iron homeostasis and ferroptosis in human diseases: Mechanisms and therapeutic prospects. Signal Transduct Target Ther 9: 271, 2024.
44. Yan HF, Zou T, Tuo QZ, Xu S, Li H, Belaidi AA and Lei P: Ferroptosis: Mechanisms and links with diseases. Signal Transduct Target Ther 6: 49, 2021.
45. Zheng Y, Yan F, He S and Luo L: Targeting ferroptosis in autoimmune diseases: Mechanisms and therapeutic prospects. Autoimmun Rev 23: 103640, 2024.
46. Li X, Xing C, Tian M, Liu B, Tong J, Yu H, Huang C, Su L, You X and Wu J: Remimazolam alleviates intracerebral hemorrhage outcomes by suppressing neuronal ferroptosis. Eur J Pharmacol 1006: 178203, 2025.
47. Lee JH: Remimazolam-expectations and concerns. Korean J Anesthesiol 78: 89-90, 2025.